Three-dimensional geophysical anatomy of an active landslide in Lias Group mudrocks, Cleveland basin, UK

J.E. Chambers*, P.B. Wilkinson, O. Kuras, J.R. Ford, D.A. Gunn, P.I. Meldrum, C.V.L. Pennington, A.L. Weller, P.R.N. Hobbs, and R.D. Ogilvy

British Geological Survey, Kingsley Dunham Centre, Nottingham, NG12 5GG, UK

*Corresponding author. Tel.: +44(0)115 936 3428; Fax: +44(0)115 936 3261; E-mail, jecha@bgs.ac.uk

Abstract

A geoelectrical investigation of a slow moving earth slide-earth flow in Lower Jurassic Lias Group rocks of the Cleveland basin, UK, is described. These mudrock slopes are particularly prone to failure and are a major source of lowland landslides in the UK, but few attempts have been made to spatially or volumetrically characterise the subsurface form of these slides. The primary aim of this study was to consider the efficacy of fully three-dimensional geoelectrical imaging for landslide investigation with reference to a geological setting typical of Lias Group escarpments. The approach described here included a reconnaissance survey phase using two-dimensional electrical resistivity tomography (ERT), resistivity mapping, self-potential (SP) profiling and mapping, followed by a detailed investigation of an area of the landslide using three-dimensional (3D) ERT and self-potential tomography (SPT). Interpretation of the geophysical data sets was supported by surface observations (aerial LiDAR and differential GPS geomorphological surveys) and intrusive investigations (boreholes and auger holes). The initial phase of the study revealed the existence of a strong SP signature at the site consistent with a streaming potential source and established the relationships between the main geological units, the geomorphologic expression of the landslide, and the resistivity of the materials in and around the study area. The 3D SPT model generated during the second phase of the study indicated drainage patterns across the landslide and preferential flow from the low permeability mud rocks into the underlying more permeable sandstone formation.

Because of favourable resistivity contrasts between the clay-rich Whitby Mudstone Formation landslide material and the underlying Staithes Sandstone Formation, the volumetric 3D ERT image allowed a number of surface and subsurface landslide features to be identified and spatially located. These included the lateral extent of slipped material and zones of depletion and accumulation; the surface of separation and the thickness of individual earth flow lobes; and the dipping in situ geological boundary between the Whitby Mudstone and Staithes Sandstone bedrock formations.

Keywords: landslide; electrical resistivity tomography (ERT); self-potential (SP); Lias

1. Introduction

The application of geophysical methods to landslide characterisation and monitoring has steadily increased in recent years because of improvements in ground imaging techniques (Jongmans and Garambois, 2007). Crucially, geophysical methods have the potential to provide spatial or volumetric information on subsurface structure and property variations. This is in contrast to mapping methods, such as remote sensing or aerial photography that are limited to providing surface information, and to intrusive methods, such as boreholes and penetration tests that provide subsurface data only at discrete locations. Geophysical methods, however, have been most effectively applied when used in conjunction with other surface and ground investigation techniques (e.g., Van Den Eeckhaut et al., 2007; Sass et al., 2008); this integrated approach is particularly important for geophysical investigations that provide physical property information rather than direct geological or geotechnical data, and so require calibration. Seismic methods and ground penetrating radar (e.g., Schrott and Sass, 2008) are now widely used, as are a range of geoelectrical methods, including resistivity and self-potential (SP), which are the focus of this study.

Geoelectrical investigations of landslides are dominated by the use of two-dimensional (2D) electrical resistivity tomography (ERT), which is a rapid and lightweight means of acquiring spatial information on ground structure and composition. Resistivity methods have proved to be successful because of the sensitivity of resistivity to changes in lithology − principally related to electric conduction on the surface of clay minerals − and moisture content (e.g., Telford et al., 1990; Shevnin et al., 2007); hence, these methods are being developed to investigate the structure of landslides in terms of compositional variations, depth to bedrock, geological boundaries and slip plane geometry (e.g., Drahor and Berge, 2006; Godio et al., 2006; Jomard et al., 2007b; Van Den Eeckhaut et al., 2007; Yilmaz, 2007; Göktürkler et al., 2008; Marescot et al., 2008; Sass et al., 2008; Erginal et al., 2009; Schmutz et al., 2009), and also the associated hydrogeological regime (e.g., Grandjean et al., 2006; Jomard et al., 2007a; Lee et al., 2008; Niesner and Weidinger, 2008; Piegari et al., 2009).

59 Several of these studies detail the investigation of clayey landslides, and are therefore particularly
60 relevant to this study. Examples include Lapenna et al. (2005) who described the use of 2D ERT to
61 successfully characterise the extent and depth of Giarrossa and Varco d'Izzo landslides, Italy, both of
62 which are rototranslational slide-earthflows. Lee et al. (2008) used ERT to contribute to the
63 development of lithological and hydrogeological models of the Lishan landslide, Taiwan, through
64 identifying the subsurface structure associated with slipped clay rich colluviums overriding slate
65 bedrock. The ERT surveys described by Schmutz et al. (2009) were applied to the investigation of the
66 Super Sauze landslide, France, which in its lower regions forms an earthflow. The study concludes
67 that ERT was an effective means of imaging the internal structure of the landslide and discriminating
68 between different lithologies.

69 Although 2D ERT is now commonly used, three-dimensional (3D) ERT has rarely been applied despite
70 being a clearly more appropriate method. Landslides are inherently 3D structures, often displaying
71 very significant spatial heterogeneity, and so in these cases 3D features to the side of 2D survey lines
72 will cause significant artefacts and inaccuracies in 2D resistivity models (Chambers et al., 2002;
73 Sjodahl et al., 2006). The dearth of examples of 3D ERT for landslide investigation is probably due to
74 the greater complexity of survey design, field deployment, and data processing that is required
75 relative to 2D imaging. One of the few studies described in the literature (Lebourg et al., 2005) used
76 3D ERT to characterise a section of the La Clapière landslide in the French Alps. The study was
77 conducted within an area of 70 x 90 m, and the resulting images were used to identify deep-seated
78 slip surfaces and related hydrogeological changes.

79 Self-potential surveys involve the measurement of naturally occurring geoelectric fields that are
80 generated in the subsurface by a range of mechanisms (Telford et al., 1990). The use of SP in
81 hydrogeological studies is concerned primarily with electrokinetic effects, also referred to as
82 streaming potentials, that are caused by the movement of fluid through porous rocks and soils (Revil
83 et al., 1999). The simplest type of SP surveys to have been applied to landslide investigations are

84 profiling (Bruno and Marillier, 2000) and mapping (Perrone et al., 2004) that have been used to
85 identify zones of negative and positive charge, which correlate with the infiltration and accumulation
86 of water in the subsurface; the SP map produced by Perrone et al. (2004) was used to investigate
87 subsurface fluid flow across the entire area of a clayey landslide with a length of 1400m and a width
88 of up to 420 m. Tomographic reconstruction of SP data is, however, beginning to be applied to image
89 subsurface charge distributions related to the hydrogeological regime within clayey landslides in 2D
90 (Lapenna et al., 2003) and 3D (Colangelo et al., 2006).

91 In this study we apply geoelectrical methods (including resistivity mapping, 2D and 3D ERT, and SP
92 profiling, mapping and tomography) to the investigation of an active landslide in the Upper Lias,
93 Whitby Mudstone Formation. The Lias Group is Lower Jurassic in age and is composed primarily of
94 argillaceous sediments, including marine limestones, shales, marls, and clays. The Group extends
95 across significant areas of western Europe, and in England and Wales it outcrops as a continuous
96 band from Dorset on the south coast to the North Yorkshire coast in the NE of England. Slopes
97 comprising Lias Group rocks are particularly prone to failure, accounting for 15% of all landslides
98 recorded in Britain (Jones and Lee, 1994). Landslides within Lias Group rocks have a wide
99 geographical distribution, at both inland and coastal outcrop, with the most common types including
100 rotations, flows, and slides as well as cambering (Hobbs et al., 2005). Within the UK, the greatest
101 concentration of landslides are found in the Upper Lias sequence with up to 42 slides per 100 km^2
102 (Hobbs et al., 2005). Despite their widespread occurrence, few, if any, studies describe the
103 application of noninvasive geophysical techniques to investigate slope failure in Lias Group rocks.

104 The landslide considered here was selected as a representative example typical of many landslides in
105 Lias Group mudrocks whose characteristics often include (Hobbs et al., 2005): a substantial thickness
106 of weak weathered mudrock underlying a more competent unit (usually sandstone or limestone); a
107 relatively low angle; shallow translational failures characterised by earth flows towards the toe and
108 rotations at the head. The primary aim of this work was to consider the efficacy of fully 3D

109 geoelectrical approaches to landslide investigation, with particular reference to the geological
110 context of the Lias Group. Interpretation and calibration of the 3D geophysical site models was
111 supported by aerial photography, geological mapping, aerial LIDAR scans, intrusive sampling, and 1D
112 and 2D geoelectrical surveys (i.e. SP profiling, resistivity and SP mapping, and 2D ERT). The improved
113 understanding of the geophysical anatomy of the landslide revealed by this study is intended to
114 inform the design of a permanent geophysical monitoring network at the site.

115

116 **2. Study area**

117 The study area is located on the northeastern edge of Sheriff Hutton Carr, a broad topographic
118 embayment on the eastern margin of the Vale of York. Sheriff Hutton Carr is bounded to the north
119 by the Lias Group escarpment and to the south by a semicontinuous ridge of Devensian till and
120 outlying Jurassic strata. Geological surveying of the York district (Ford, in press) proposed that
121 original drainage from this area was toward the SW. However, during the Devensian, an ice-marginal
122 lake (Lake Mowthorpe - see glaciolacustrine deposits on the western edge of geological map in Fig.
123 1) developed as meltwater from the NW and surface-water runoff from the escarpment was
124 confined between the escarpment and the ice sheet to the south. A spill point was reached at the
125 eastern edge of the lake, resulting in the rapid incision of a north-south aligned gorge and the
126 establishment of the modern-day drainage system along Bulmer Beck. This steep-sided gorge is
127 flanked by the Whitby Mudstone Formation and is subject to multiple landslides (Fig. 1). Postglacial
128 landslides may have periodically dammed off the gorge, resulting in the reestablishment of Lake
129 Mowthorpe.

130 The escarpment is underlain by a shallow marine mudstone-dominated succession of Lower Jurassic
131 age comprising, in ascending order, the Redcar Mudstone (RMF), Staithes Sandstone and Cleveland
132 Ironstone (SSF), and Whitby Mudstone Formations (WMF). The last formation is the principal source

of slope failure at the site and in the surrounding area (Fig. 1). The escarpment is capped by the Dogger Formation of Middle Jurassic age; although thinly developed, this limestone- and sandstone-dominated unit represents a potential aquifer above the WMF and is a principal component of head deposits on the escarpment. The bedrock succession displays a regional dip of 1° to 2° to the north on the southern edge of the Cleveland Basin, although locally beds can dip by as much as 7°. The RMF comprises grey, silty, calcareous, and sideritic mudstone with thin shelly limestones (Rawson and Wright, 1995). The RMF is estimated to be up to 175 m thick, although only the upper 25 m are exposed in the lower part of the escarpment. The formation is characterised by poorly drained clay soil. The upper boundary of the formation displays a gradational transition to the SSF. The SSF comprises ferruginous, micaceous siltstone with fine-grained sandstone and thin mudstone partings. It is heavily bioturbated and locally contains siderite and small pyrite masses (Gaunt et al., 1980). The formation is about 20 m thick and is associated with well-drained loam soil in the middle part of the escarpment. The upper boundary of the formation is marked by a transition to mudstone of the WMF, which is composed of grey to dark grey mudstone and siltstone with scattered bands of calcareous and sideritic concretions. The WMF is ~ 25 m thick, with a sharp upper boundary marked by the erosive base of the Dogger Formation. The formation is commonly deeply weathered and poorly consolidated near to the ground surface, giving rise to poorly drained clay soil. The escarpment is capped by the Dogger Formation, forming an extensive dipslope extending to the north of the site. The formation is characterised by calcareous sandstone and ferruginous limestone including rounded clasts of micritic limestone. The Dogger Formation occupies hollows in the angular unconformity with the WMF and ranges considerably in thickness across the region to attain a local maximum of 8 m (to the north of the site). The Dogger Formation gives rise to free-draining sandy soil rich in gravel- to cobble-size rock fragments. In common with the surrounding area, the bedrock succession at the escarpment is overlain by a thin layer of head. This deposit is characterised by gravelly, sandy, silty clay with occasional organic inclusions, representing locally derived material, reworked by a combination of near-surface processes including hillwash, slope failure, and soil

159 creep. The thickness of head deposits is highly variable, ranging from 0.2 to 1.3 m, generally
160 increasing toward the base of the escarpment. These thin and locally discontinuous head deposits
161 are not shown on Fig. 1.

162 The landslide is a very slow to slow moving composite multiple earth slide–earth flow, according to
163 the classification scheme proposed by Cruden and Varnes (1996), with maximum rates of movement
164 observed in recent years in the order of 2 m/y. Movements were monitored by repeated Real Time
165 Kinematic (RTK) GPS measurents of marker peg locations across the landslide over a period of two
166 years. Maximum rates of movement occurred towards the fronts of the lobes. The principal
167 movements have typically occurred during winter months when the slope is at its wettest. The
168 landslide extends laterally along the escarpment for more than 1 km covering and area of
169 approximately 10 hectares, with much of it hidden by woodland. The section of the landslide
170 described in this study is situated within a grassed area with a width of 250 m and a total length of ~
171 180 m. A geomorphological map of the study area is shown in Fig. 2A, in which concave and convex
172 breaks of slope have been mapped, with line work indicating whether the break in slope was
173 rounded or sharp. The map was created using a combination of stereophotogrammetry, analysis of
174 aerial LiDAR data (see base layer in Fig. 2A), and line work generated from ground based RTK-GPS
175 measurements. The GPS survey was used, in particular, to capture those features with a sharp break
176 in slope, such as the main scarp, and fresh ruptures in the foot of the landslide. The upper sections
177 to the north are characterised by rotational slides with multiple minor scarps and cracking within the
178 WMF, which evolve into heavily fissured earth flows that form discrete lobes of slipped material
179 overriding the SSF bedrock to the south. Multiple stacked phases of earth flow activity associated
180 with the lobes are apparent; toward the base of the slope stabilised and degraded earth flows are in
181 evidence, whilst the upper sections of the lobes are characterised by fresh ruptures from ongoing
182 earth flow development.

183 The hydrology of the site is complex and not well constrained. The interface between the SSF and
184 the less permeable RMF at the base of the slope (Fig. 2) defines a spring line that is active for most of
185 the year. During wet periods, sag ponds develop within the backward-tilted section below the main
186 scarp (Fig. 2A) and water seeps from the fronts of the lobes toward the base of the slope. Intrusive
187 investigations (i.e. drilling and hand augering; Fig. 3) across the study area have revealed significant
188 heterogeneity and lithological variability in both the slipped and in-situ material. During augering
189 multiple perched water levels and horizons on which seepages are occurring within the WMF and
190 SSF bedrock were observed in the slipped material within the lobes.

191

192 **3. Methodology**

193 Initial geoelectrical surveying across the site was undertaken using 2D ERT, SP profiling, and mobile
194 resistivity mapping. A section of the site was then selected for more detailed investigation using 3D
195 ERT, SP mapping, and SPT surveys. This area extended from the back scarp to beyond the toe of the
196 lobes on the eastern side of the site and was selected as it was representative of the wider site, it
197 covered the enter length of the slip, and it included some of the most active areas of the landslide.

198 *3.1. Electrical resistivity tomography (ERT)*

199 Geoelectrical imaging techniques such as ERT are now widely used for studying environmental and
200 engineering problems (Pellerin, 2002). Electrical resistivity tomography produces spatial or
201 volumetric models of subsurface resistivity distributions, from which features of contrasting
202 resistivity may be located and characterised. Methodologies for 2D and 3D ERT data collection and
203 modelling are described widely in the literature (e.g. Dahlin et al., 2002; Lapenna et al., 2005), so
204 only a short summary is provided here.

205 During the course of an ERT survey, multiple electrical resistance measurements are made. In this
206 case ERT data were collected using an AGI SuperSting R8 IP system attached to stainless steel
207 electrodes via multicore cables. The locations of the four 2D ERT survey lines and the 3D ERT imaging
208 area are shown in Fig. 2B. Two-dimensional ERT data were collected on four north-south trending
209 survey lines, shown as lines 1, 2, 3, and 4 with lengths of 189, 477, 186, and 180 m, respectively. The
210 extended line 2 was deployed to capture the full geological succession in the area; its full extent is
211 not shown in Fig. 2B. The 3D ERT data set was collected using a set of five survey lines within an area
212 of 38 x 147.25 m (Fig. 2B); lines were oriented parallel to the long axis of the survey area, with along-
213 line electrode separations of 4.75 m and interline separations of 9.5 m. A dipole-dipole configuration
214 was employed throughout the survey for both 2D and 3D surveys, with the exception of line 4, for
215 which a Wenner-type configuration was used. The 2D dipole-dipole lines (lines 1 to 3) were surveyed
216 using dipole lengths (a) of 3, 6, 9, 12, and 15 m and dipole separations (na) of 1a to 8a. For the 3D
217 survey, data were collected using dipole sizes of 4.75, 9.5, 14.25, and 19 m and n levels of 1 to 8. The
218 dipole-dipole array has many advantages: it is a well-tested array with good resolving capabilities
219 (Chambers et al., 2002; Dahlin and Zhou, 2004); it does not require the use of a remote electrode; it
220 can efficiently exploit the multichannel capability of modern ERT instruments; and crucially, it
221 enables reciprocal measurements to be collected. In this case, full sets of reciprocal measurements
222 were collected for both the 2D and 3D dipole-dipole surveys. Reciprocal measurements provide a
223 particularly effective means of assessing data quality and determining robust and quantitative data
224 editing criteria (e.g. Dahlin and Zhou, 2004). For a normal four-electrode measurement of transfer
225 resistance (ρ_n), the reciprocal (ρ_r) is found by interchanging the current and potential dipoles.
226 Reciprocal error $|e|$ is defined here as the percentage standard error in the average measurement,

227 $$|e| = 100 \times |\rho_n - \rho_r| / (\rho_n + \rho_r) \quad (1)$$

228 For lines 1, 2, and 3, for which reciprocal measurements were collected, 83, 95, and 93% of the
229 respective data sets had errors of < 5%; whilst for the 3D dataset, 99.8% of the data had a reciprocal

error of < 5%. Data points with a reciprocal error of > 5% were removed from the data sets, and the reciprocal errors were used to weight the data during the inversion.

In brief, the aim of the inversion process is to calculate a model that satisfies the observed data. A starting model is produced, which in these cases was a homogeneous half-space, for which a response is calculated and compared to the measured data. The starting model is then modified in such a way as to reduce the differences between the model response and the measured data; these differences are quantified as a mean absolute misfit error value. This process continues iteratively until acceptable convergence between the calculated and measured data is achieved, or until the change between error values calculated for consecutive iterations becomes insignificant. The 2D and 3D ERT field data were inverted using l_1-norm implementations (Loke and Lane, 2002) of the regularized least-squares optimization method (Loke and Barker, 1995, 1996). The forward problem was solved using the finite-element method, in which node positions were adjusted to allow topography to be taken into account in the inversion process (Loke, 2000).

In general, a range of different models with identical responses could be obtained from the field data; this is due to its necessarily incomplete nature. The problem of nonuniqueness is exacerbated with increasing depth of investigation because the model in these regions is less well constrained by the data. The model that best satisfies the l_1-norm smoothness criterion is therefore chosen, which favours sharp boundaries between regions of different resistivity. Despite this, the lack of completeness in the data will cause the sharpness, position, and contrast of these boundaries to be more poorly resolved with increasing depth. Therefore, the ERT models can provide only an approximate guide to the true resistivity and geometry of subsurface features (Olayinka and Yaramanci, 2000); and hence, calibration using intrusive sampling is highly desirable.

3.2. Mobile resistivity mapping

253 Mobile resistivity mapping was undertaken using the automated resistivity profiling (ARP) technique,
254 which uses a patented multielectrode device (Geocarta SA, France) in order to make direct current
255 (DC) measurements of subsurface electrical resistivity along profiles with the aim of producing
256 horizontal property maps (Dabas and Favard, 2007; Dabas, 2009). Electrical mapping using DC
257 resistivity methods (e.g. Panissod et al., 1998; Kuras et al., 2007) has advantages over methodologies
258 based on electromagnetic (EM) induction from smaller uncertainties in sensor calibration and
259 greater control over the depth of investigation (Dabas and Tabbagh, 2003). In its basic form, ARP
260 measures the apparent resistivity (ρa) for three different equatorial array configurations, each with a
261 greater separation between current and potential dipoles than the last and, hence, with a greater
262 measurement volume and depth of investigation. The ARP electrodes are wheel-mounted and are
263 rolled along the surface where they are automatically inserted into the ground, acting as current and
264 potential dipoles. Apparent resistivity maps can provide information on the spatial variability of soil
265 properties such as texture, clay content, moisture, stoniness, and depth to substratum (Samouelian
266 et al., 2005). The ARP sensor array is pulled by an all-terrain vehicle, thus allowing apparent
267 resistivity data to be acquired simultaneously for three separate depth profiles (0-0.5, 0-1, and 0-2 m
268 below ground level). The use of real-time kinematic GPS navigation within the system enables on-
269 site navigation and the acquisition of spatially accurate data in real time. This survey method
270 provides highly mobile and self-contained data acquisition over areas of ~ 40 ha d^{-1}. Typical site
271 coverage follows a grid of parallel survey lines in a bidirectional pattern, guided by on-board
272 navigation. For this study however, the survey lines were necessarily less regular because of the
273 complex and steep terrain. Data processing involved the application of a 1D median filter along each
274 transect, followed by a bicubic spline interpolation on a 2.5-m regular mesh.

275 *3.3. Self potential (SP) profiling, mapping and tomography*

276 The causative mechanisms of SP anomalies include thermal, electrochemical, and electrokinetic
277 phenomena as well as voltages resulting from anthropogenic sources. Applications related to these

various mechanisms range from investigations of geothermal activity (e.g. Yasukawa et al., 2005), where SP signatures generated by thermal and electrokinetic effects are observed, to mineral prospecting (e.g. Heinson et al., 2005) and contaminated land studies (e.g. Minsley et al., 2007) where electrochemical effects often dominate. With no obvious sources of cultural noise or thermoelectric or electrochemical effects, the primary cause of SP at this site is likely to be streaming potentials related to groundwater movement. Streaming potentials are produced due to differences in mobility of ions in the groundwater. In general, the region to which groundwater is flowing is more electrically positive than the source area.

Self potential measurements were undertaken along profiles occupying the four lines used for 2D ERT surveys and within an area broadly coincident with the 3D ERT survey area (Fig. 2B). The separation between measurement points along the four lines was 5 m. The SP mapping area comprised five lines parallel to the long axis of the survey area, with measurement points at 5-m intervals and a line separation of 10 m. Data acquisition was achieved with a high impedance voltmeter and a pair of Pb/PbCl (Petiau, 2000) electrodes, used as a reference and a roving electrode, respectively. Electrode positions were prepared in advance by hand-auguring shallow holes, < 0.1 m deep, which were filled with bentonite slurry to ensure good contact between the electrode and the ground. The reference electrode was established at a fixed point, and the roving electrode was moved across the survey area to the prepared positions; at each survey point the potential difference between the electrodes was recorded. During the surveys of lines 1, 3, and 4, the reference electrode was positioned at the midpoint of the respective profile at a distance of ~ 1 m from the line. Measurements on line 2 were carried out in three sections with the reference electrode located at 100, 300, and 400 m, respectively; measured voltage offsets relative to section 1, resulting from the use of different reference electrode positions for sections 2 and 3, were removed to produce a consistent profile. The SP mapping area was surveyed with a single reference electrode position, located in the centre. Prior to data collection, the electrodes were placed in a water bath to correct for drift. During the line surveys, each electrode position was occupied twice

by traversing down (forward) and then immediately back up (reverse) each line. In the case of the mapping area, the roving electrode was migrated from the northwestern corner of the grid in a snaking north-south pattern to the southeastern corner (forward) and then back to the northwestern corner (reverse). By collecting repeat measurements in this way, the time dependent SP drift could be assessed. The calculated means and standard deviations (SD) of the drift for lines 1, 2, 3, and 4 were 0.8 mV (SD 0.6 mV), 1.7 mV (SD 1.3 mV), 1.4 mV (SD 1.1 mV), and 1.6 mV (SD 1.1 mV), respectively, and 2.1 mV (SD 2.1 mV) for the SP mapping area. In this paper, the SP survey data are presented as 1D profiles for each of the lines and as a 2D contour plot within the mapping area.

In addition, the SP mapping data were used to determine the likely 3D distribution of electrical charge accumulation in the subsurface. This was achieved by applying an SPT algorithm (Patella, 1997a, b, 1998), which calculates the cross-correlation between the observed surface potentials and the potential from a hypothetical scanning test charge. This technique has successfully been used to determine the subsurface charge distributions of the Vesuvius volcano (Patella, 1997b) and the Giarrossa (Lapenna et al., 2003) and Varco d'Izzo landslides (Perrone et al., 2004). The cross-correlation is interpreted as a Charge Occurrence Probability (COP) η. This lies in the range $-1 \leq \eta \leq 1$, where a large magnitude indicates an increased likelihood that charge has accumulated at that point and a negative value simply implies that the accumulated charge is negative.

The self-potential tomograms in this paper were produced by calculating $\eta(x, y)$ for a number of discrete depth levels (z). The algorithm is based on a modification of the above technique that allows for the inclusion of topography (Patella, 1997b, 1998). Furthermore, higher order numerical approximations to the cross-correlation integrals and derivatives of V were used (Wilkinson et al., 2005) to improve the contrast between low and high values of η in the tomograms.

4. Results and interpretation

4.1. 1D (SP Profiles) and 2D (2D ERT, ARP and SP Map) Reconnaissance Surveys

The 2D ERT models generated from survey lines 1 to 4 are shown in Fig. 4. Good convergence between the measured data and the models was achieved, as indicated by mean absolute misfit error values of 1.0, 0.7, 0.8, and 2.0%, respectively. The principal geological formations can be inferred from the models on the basis of contrasting resistivities. The full geological succession associated with the site is most clearly seen in the longest line, line 2, that extends outside of the study site to both the north and the south. Both the RMF and the WMF are characterised by resistivities of < 20 Ωm, which are consistent with high clay content. The SSF, however, displays higher resistivities ranging from ~ 30 to 200 Ωm, reflecting a lithology dominated by silts and sands and significant geoelectrical heterogeneity. Factors causing the observed heterogeneity are likely to include both moisture content and lithology. In particular, the high near surface resistivities (e.g. Fig. 4, Line 2, x = 150 to 200 m) are probably related to lower moisture contents because of drainage into lower levels of the formation. Intrusive investigations in the SSF at the study site have confirmed that it is a complex deposit (Fig. 3) displaying very significant variation in grain size and moisture content, with multiple perched water levels and seepages. At the base of the slope within the area formerly occupied by Lake Mowthorpe (Fig. 4, line 2), slightly more resistive deposits (20 to 30 Ωm) appear at the surface. This feature is unlikely to be related to bedding within the RMF as it does not follow the general dip of the formation to the north. Instead, these elevated resistivities may be indicative of lake deposits, which have been observed from intrusive investigations on the valley floor to the SW of the study site. The results of the line 2 ERT survey indicate that these deposits extend further to the east than indicated by the geological mapping (Fig. 1).

The good resistivity contrast between the SSF and the mudstone allows the general dip of the formations to be distinguished within the resistivity models; and significantly, it provides a means of identifying the extent and thickness of slipped WMF overriding the SSF, as observed particularly on lines 2, 3, and 4 (Fig. 4). In section, the lobes appear in the images as low resistivity (blue-green)

353 regions encroaching as a thin surface layer onto high resistivity SSF (orange-red); these features are
354 seen particularly on lines 2 and 3 (Fig. 4). The horizontal extent of the WMF is clearly revealed by the
355 resistivity contrast with the SSF shown in the ARP resistivity map (Fig. 5). The RMF is not apparent on
356 the southern edge of the ARP map, which may be due to a thin cover of resistive head deposits
357 obscuring this boundary. Coverage of the study site was limited by the terrain that in places, as
358 indicated by absent data, was too steep or rough to allow access to the ARP array. Those areas
359 covered by the survey do, however, reveal the development of a number of lobes of slipped
360 material, which are consistent with those identified in the geomorphological map (Fig. 2A). The most
361 clearly defined lobes are those seen on the eastern half of the study site where ARP coverage was
362 most complete.

363 The SP profiles for lines 1 to 4 display increasingly positive values from the top of the slope to the
364 base, with ranges of 15, 17, 20, and 25 mV respectively. Comparison of the forward and reverse SP
365 measurements reveals a temporal drift in SP of up to 3 mV over a period of several minutes. The
366 general trend of increasingly positive SP downslope is consistent with a streaming potential
367 signature produced by infiltration at the top of the slope and accumulation at the base (e.g. Perrone
368 et al., 2004). The trend of increasingly positive SP values is interrupted at the front of the active
369 lobes and at the base of the slope. At these locations, surface discharge of water was observed; the
370 former being related to seepages directly from disturbed material at the tip of the active lobes (lines
371 2 and 4, Fig. 4), and the latter being related to the spring line at the interface between the SSF and
372 the underlying and less permeable RMF (line 2, Fig. 4).

373 The SP map (Fig. 6A) comprises a similar range of measured voltages, varying from 0 mV at the top
374 of the slope to 17 mV at the base, which is again consistent with a streaming potential signature. The
375 close relationship between landslide morphology and flow is indicated by the distribution of the
376 most positive voltages associated with accumulation at the front of the active lobes and in the gully
377 region between the two lobes.

4.2. 3D Imaging

The 3D ERT model is shown as a series of north-south trending vertical sections (Fig. 7), a plan view of surface resistivities (Fig. 8), and as a volumetric 3D image shown in its geographical context with the 2D ERT models of lines 1 to 4 (Fig. 9). Good convergence between the measured data and the 3D model was achieved as indicated by a mean absolute misfit error of 0.7%. Calibration of the resistivity model and the identification of interfaces between the geological formations and between the slipped WMF and in situ SSF has been achieved using intrusive data generated from auguring within this area; auger logs and locations have been included along with the 3D ERT model shown in Fig. 7 and Fig. 8, respectively. The succession from low resistivity RMF, to more resistive SSF, to low resistivity WMF is clearly displayed and is consistent with that observed in both the 2D ERT and ARP resistivity mapping surveys (e.g. Figs. 5 and 9). The interface between the SSF and the WMF indicates a dip of ~ 5° to the north (Fig. 7). As with the 2D ERT models (Fig. 4), significant heterogeneity is observed in the SSF. The WMF is significantly more homogeneous, although a band of relatively high resistivities (15 to 20 Ωm), striking in an approximately east-west direction in close association with the back scarp, can be observed (Fig. 8). This may indicate a slightly more silt rich horizon or may be a function of better drainage, and hence lower moisture content, in the steep face of the main scarp.

Variation in the thickness of slipped WMF within the 3D ERT model can be seen in Fig. 7 as a progression from the western lobe, with a thickness of up to 4.5 m (Fig. 7, x = 0 m), to the gully region between lobes where slipped material is absent (Fig. 7, x = 19 m), and onto the eastern lobe with a thickness of up to 5 m of slipped WMF (Fig. 7, x = 38 m). The low surface resistivities (blue-green) of the 3D ERT model for y = < 80 m (Fig. 8) show the distribution of slipped WMF of the eastern and western lobes. Calibration using the intrusive data has allowed an improved interpretation of the extent of the landslide within the 3D ERT survey area. In this case, imaging of the buried interface between the SSF and WMF has allowed the extent of the zones of depletion and zones of accumulation to be accurately determined.

403 The 3D SP tomogram reveals a strong concentration of positive COP in the gully region in-between
404 and toward the front of the active lobes (Fig. 6B), indicating relatively little drainage through the
405 slipped WMF of the lobes into the SSF. Instead, the 3D COP suggests that the primary flows are
406 downslope drainage and runoff from the relatively impermeable WMF and accumulation in the SSF
407 where it is exposed at the surface. Preferential charge accumulation, and hence drainage, into the
408 SSF compared to the WMF is indicated by the persistence of positive COP with depth where the SSF
409 is exposed.

410

411 **5. DISCUSSION**

412 The combined use of 2D ERT and ARP surveys has provided complementary data sets with which to
413 assess the landslide structure. The 2D ERT has defined the position of key geological interfaces and
414 the thickness of the foot of the landslide, whilst the ARP survey provided a high resolution map of
415 the lateral extent of the slipped material. The reconnaissance data provided by these techniques
416 established the relationships between the main geological units, the geomorphologic expression of
417 the landslide, and the geophysical properties of the materials associated with the landslide. The 3D
418 ERT survey combined the advantages of the 2D ERT and ARP surveys. It has provided depth
419 information that, unlike the 2D ERT models, is fully volumetric and less influenced by 3D artefacts
420 that can affect 2D models. In practice, a combination of 2D and targeted 3D surveys may provide a
421 good compromise between coverage and resolution (e.g. Fig. 9).

422 The effectiveness of resistivity methods for investigating the structure of landslides is dependent on
423 the existence of good resistivity contrasts between in situ and slipped materials (e.g. Jongmans and
424 Garambois, 2007; Bichler et al., 2004). In this case, ERT has revealed the 3D form of major geological
425 interfaces and has provided volumetric images of the foot of the landslide because of the good
426 resistivity contrast between the WMF and the SSF. Specifically, the 3D ERT model has revealed the

bedrock succession dipping ~ 5°, which is significantly more than the regional dip of 1° to 2° but is, nevertheless, consistent with other observed dips in the area. Furthermore, the interface between the WMF and SSF identified in the model is ~ 50 m higher up the slope than identified in earlier geological maps of the area (British Geological Survey, 1983); results from this survey and additional auguring have informed the most recent geological map of the area (Ford, in press, Fig. 1). However, a number of key structures were not successfully imaged using 3D ERT; these included the surface of rupture and the subsurface continuations of the fault scarps and the slip planes between the multiple stacked earth flows comprising the lobes. This was because these features occurred wholly within the WMF, which because of its relatively homogenous resistivity distribution did not result in the sufficient resistivity contrasts for these structures to be defined. The strengths and limitations of 3D ERT discussed here are likely to be pertinent for many other similar geological settings. In the context of Lias Group rocks, scarps comprising failing mudstones overlying more resistive siltstone, sandstone, or limestone formations are commonplace; therefore the application of ERT for landslide investigation in these settings is likely to be a useful investigative tool. The detection of slip planes and faults within clay-rich materials will continue, in many cases, to be a significant challenge for geophysical ground imaging methods.

Self potential profiling, mapping, and tomography have provided a snapshot of hydrogeological conditions within the landslide during the winter period when the landslide is at its wettest and when most movement occurs. The information provided by SP is consistent with drainage patterns predicted from geomorphological and geological analysis of the site; i.e., drainage is controlled by the topography with accumulations of moisture at the front of active lobes and between lobes, and springs occur at the interface between the SSF and the less permeable RMF. The SP signature seen here is approximately an order of magnitude lower than those observed in other landslide studies (Bruno and Marillier, 2000; Lapenna et al., 2003; Perrone et al., 2004); this is almost certainly due to this study being concerned with a lowland landslide with relatively small slope lengths and shallow gradients and, therefore, lower flow rates compared to these previous studies. The major benefits of

SP for landslide investigation are likely to be realised through time-lapse monitoring (Colangelo et al., 2006), where seasonal variations in groundwater movement, which are likely to be related to slope failure events, can be investigated. The observed streaming potential signatures suggest that permanently installed SP monitoring instrumentation would be worthwhile for studying landslide hydrology at this site.

Indications of moisture content variations within the landslide are not readily apparent from the 3D ERT model, as it is impossible to differentiate the influence of lithology and temperature from moisture content in a static one-off image. However, analysis of moisture content variation using resistivity could be achieved through the collection of time-lapse data and the generation of differential images in which the effects of geological heterogeneity are eliminated, thereby allowing moisture-induced resistivity changes to be quantitatively assessed. Future work at this site, which will build on the analysis of landslide structure and geophysical properties presented in this study, will involve the deployment of a geophysical monitoring network (e.g. Supper and Römer, 2003; Lebourg et al., 2005) to investigate the hydrogeological regime associated with the landslide. The aim of this future work will be to investigate whether geophysical methods can identify hydrogeological precursors to slope failure.

6. Conclusions

The integrated use of geoelectrical methods in this case has revealed significant 3D structures associated with the landslide. The geophysical results are consistent with geological, geomorphological and hydrogeological information determined or inferred from other sources, such as aerial LiDAR, differential GPS measurements, and intrusive investigations. Cross-correlation of these various lines of evidence allowed the geophysical images to be calibrated, and relationships between lithological and geophysical properties to be established.

Whilst 2D ERT and resistivity mapping approaches have provided rapid reconnaissance level data for the site, a fully 3D ERT model of a section of the landslide gave detailed volumetric information on the structure of the bedrock and the foot of the landslide, as well as combining many of the advantages of 2D ERT and mapping. Likewise, 3D modelling of the SP data gave an indication of the accumulation of groundwater within the subsurface, thereby providing an improved understanding of fluid flow at the site beyond that gained from SP profiling and mapping alone. For inherently 3D structures, such as landslides, fully volumetric geophysical approaches to subsurface characterisation are clearly preferable.

The success of resistivity methods in this case was primarily due to the strong resistivity contrasts between the weathered mudrock and the more competent underlying coarser grained silt and sandstones. These contrasts were used to map the spatial extent of low resistivity landslide material overriding the more resistive bedrock, to determine the interface between the zones of depletion and accumulation, to determine the thickness of the developing lobes, and to establish the dip of the bedrock formations. Where significant contrast did not exist, landslide structure was not revealed. Of particular significance was the back scarp located in the WMF, which was not identified from the geoelectrical data due to insufficient image resolution or contrast in electrical properties. The geological context considered here is typical of many situations in Upper Jurassic formations in which weak mudrocks are sliding over coarser more competent and permeable formations. Consequently, the successful application of 3D geoelectrical tomography methods in this study provides a basis for their wider application to the investigation of landsliding within the Lias Group.

Acknowledgements

We would like to extend our sincerest gratitude to Mr. and Mrs. Gibson (the landowners) for their involvement and cooperation in the research. The aerial LiDAR data is used with the permission of

3D Laser Mapping Limited. This paper is published with the permission of the Executive Director of the British Geological Survey (NERC).

References

Bichler, A., Bobrowsky, P., Best, M., Douma, M., Hunter, J., Calvert, T., Burns, R., 2004. Three-dimensional mapping of a landslide using a multi-geophysical approach: the Quesnel Forks landslide. Landslides 1(1), 29-40.

British Geological Survey, 1983. York, England and Wales. Sheet 63, Solid and Drift, 1:50,000. Ordnance Survey for Institute of Geological Sciences, Southampton UK.

Bruno, F., Marillier, F., 2000. Test of high-resolution seismic reflection and other geophysical techniques on the Boup Landslide in the Swiss Alps. Surveys in Geophysics 21(4), 333-348.

Chambers, J.E., Ogilvy, R.D., Kuras, O., Cripps, J.C., Meldrum, P.I., 2002. 3D electrical imaging of known targets at a controlled environmental test site. Environmental Geology 41(6), 690-704.

Colangelo, G., Lapenna, V., Perrone, A., Piscitelli, S., Telesca, L., 2006. 2D Self-potential tomographies for studying groundwater flows in the Varco d'Izzo landslide (Basilicata, southern Italy). Engineering Geology 88(3-4), 274-286.

Cruden, D.M., Varnes, D.J., 1996. Landslide types and processes. In: Turner, A.K., Schuster, R.L. (Eds.), Landslides, Investigation and Mitigation. Special Report 247, National Academy Press, Washington, DC, pp. 36-71.

Dabas, M., 2009. Theory and practice of the new fast electrical imaging system ARP. In: Campana S., Piro S. (Eds), Seeing the Unseen. Geophysics and Landscape Archaeology. CRC Press, London, pp. 105-126.

523 Dabas, M., Favard, A., 2007. Rapid Electrical Soil Mapping at Shelford, Nottinghamshire, and Five
524 Further Sites across the UK. Phase 2 ARP Survey – February 2007, Geocarta commissioned report for
525 the British Geological Survey, Nottingham, UK.

526 Dabas, M. and Tabbagh, A., 2003. A comparison of EMI and DC methods used in soil mapping –
527 theoretical considerations for precision agriculture. 4th European Conference on Precision
528 Agriculture, Berlin, Germany.

529 Dahlin, T., Zhou, B., 2004. A numerical comparison of 2D resistivity imaging with 10 electrode arrays.
530 Geophysical Prospecting 52(5), 379-398.

531 Dahlin, T., Bernstone, C., Loke, M.H., 2002. A 3-D resistivity investigation of a contaminated site at
532 Lernacken, Sweden. Geophysics 67(6), 1692-1700.

533 Drahor, M.G., Berge, M.A., 2006. Geophysical investigations of the Seferihisar geothermal area,
534 western Anatolia, Turkey. Geothermics 35(3), 302.

535 Erginal, A.E., Ozturk, B., Ekinci, Y.L., Demirci, A., 2009. Investigation of the nature of slip surface using
536 geochemical analyses and 2-D electrical resistivity tomography: a case study from Lapseki area, NW
537 Turkey. Environmental Geology 58(6), 1167-1175.

538 Ford, J.R., in press. Geological Map of the High Stittenham Area (Sheet SE66NE). British Geological
539 Survey, Nottingham, UK.

540 Gaunt, G.D., Ivimey-Cook, H.C., Penn, I.E., Cox, B.M., 1980. Mesozoic Rocks Proved by IGS Boreholes
541 in the Humber and Acklam Areas. Institute of Geological Sciences, Nottingham, UK.

542 Godio, A., Strobbia, C., De Bacco, G., 2006. Geophysical characterisation of a rockslide in an alpine
543 region. Engineering Geology 83(1-3), 273-286.

544 Göktürkler, G., Balkaya, C., Erhan, Z., 2008. Geophysical investigation of a landslide: the Altindag
545 landslide site, Izmir (western Turkey). Journal of Applied Geophysics 65(2), 84-96.

546 Grandjean, G., Pennetier, C., Bitri, A., Meric, O., Malet, J.P., 2006. Characterization of the internal
547 structure and the hydric state of clayey-marly landslides through geophysical tomography: example
548 of the Super-Sauze earthflow (French South Alps). Comptes Rendus Geoscience 338(9), 587-595.

549 Heinson, G., White, A., Robinson, D., Fathianpour, N., 2005. Marine self-potential gradient
550 exploration of the continental margin. Geophysics 70(5), G109.

551 Hobbs, P.R.N. et al., 2005. The Engineering Geology of UK Rocks and Soils: The Lias Group. British
552 Geological Survey IR/05/008, Nottingham, UK.

553 Jomard, H., Lebourg, T., Binet, S., Tric, E., Hernandez, M., 2007a. Characterization of an internal
554 slope movement structure by hydrogeophysical surveying. Terra Nova 19(1), 48-57.

555 Jomard, H., Lebourg, T., Tric, E., 2007b. Identification of the gravitational boundary in weathered
556 gneiss by geophysical survey: La Clapiere landslide (France). Journal of Applied Geophysics 62(1), 47-
557 57.

558 Jones, D.C.K., Lee, E.M., 1994. Landsliding in Great Britain. HMSO, London.

559 Jongmans, D., Garambois, S., 2007. Geophysical investigation of landslides: a review. Bulletin De La
560 Societe Geologique De France 178(2), 101-112.

561 Kuras, O., Meldrum, P.I., Beamish, D., Ogilvy, R.D., Lala, D., 2007. Capacitive resistivity imaging with
562 towed arrays. Journal of Environmental and Engineering Geophysics 12, 267-279.

563 Lapenna, V., Lorenzo, P., Perrone, A., Piscitelli, S., Sdao, F., Rizzo, E., 2003. High-resolution
564 geoelectrical tomographies in the study of Giarrossa landslide (southern Italy). Bulletin of
565 Engineering Geology and the Environment 62(3), 259-268.

566 Lapenna, V., Lorenzo, P., Perrone, A., Piscitelli, S., Rizzo, E., Sdao, F., 2005. 2D electrical resistivity
567 imaging of some complex landslides in the Lucanian Apennine chain, southern Italy. Geophysics
568 70(3), B11-B18.

569 Lebourg, T., Binet, S., Tric, E., Jomard, H., El Bedoui, S., 2005. Geophysical survey to estimate the 3D
570 sliding surface and the 4D evolution of the water pressure on part of a deep seated landslide. Terra
571 Nova 17(5), 399-406.

572 Lee, C.C., Yang, C.H., Liu, H.C., Wen, K.L., Wang, Z.B., Chen, Y.J., 2008. A study of the hydrogeological
573 environment of the lishan landslide area using resistivity image profiling and borehole data.
574 Engineering Geology 98(3-4), 115-125.

575 Loke, M.H., 2000. Topographic Modelling in Electrical Imaging Inversion. EAGE 62nd Conference and
576 Technical Exhibition, Glasgow, Scotland.

577 Loke, M.H., Barker, R.D., 1995. Least-squares deconvolution of apparent resistivity pseudosections.
578 Geophysics 60(6), 1682-1690.

579 Loke, M.H., Barker, R.D., 1996. Practical techniques for 3D resistivity surveys and data inversion.
580 Geophysical Prospecting 44(3), 499-523.

581 Loke, M.H., Lane, J.W., 2002. The use of constraints in 2D and 3D resistivity modelling. 8th Meeting
582 of the European Section of the Environmental and Engineering Society, Aveiro, Portugal, p. 4.

583 Marescot, L., Monnet, R., Chapellier, D., 2008. Resistivity and induced polarization surveys for slope
584 instability studies in the Swiss Alps. Engineering Geology 98(1-2), 18-28.

585 Minsley, B.J., Sogade, J., Morgan, F.D., 2007. Three-dimensional self-potential inversion for
586 subsurface DNAPL contaminant detection at the Savannah River Site, South Carolina. Water
587 Resources Research 43 (4), W04429.

588 Niesner, E. and Weidinger, J.T. 2008. Investigation of a historic and recent landslide area in
589 Ultrahelvetic sediments at the northern boundary of the Alps (Austria) by ERT measurements. The
590 Leading Edge 27, 1498-1509.

591 Olayinka, A.I., Yaramanci, U., 2000. Assessment of the reliability of 2D inversion of apparent
592 resistivity data. Geophysical Prospecting 48(2), 293-316.

593 Panissod, C., Dabas, M., Hesse, A., Jolivet, A., Tabbagh, J., Tabbagh, A., 1998. Recent developments
594 in shallow-depth electrical and electrostatic prospecting using mobile arrays. Geophysics 63(5),
595 1542-1550.

596 Patella, D., 1997a. Introduction to ground surface self-potential tomography. Geophysical
597 Prospecting 45(4), 653-681.

598 Patella, D., 1997b. Self-potential global tomography including topographic effects. Geophysical
599 Prospecting 45(5), 843-863.

600 Patella, D., 1998. Erratum. Geophysical Prospecting 46, 103.

601 Pellerin, L., 2002. Applications of electrical and electromagnetic methods for environmental and
602 geotechnical investigations. Surveys in Geophysics 23(2-3), 101-132.

603 Perrone, A., Iannuzzi, A., Lapenna, V., Lorenzo, P., Piscitelli, S., Rizzo, E., Sdao, F., 2004. High-
604 resolution electrical imaging of the Varco d'Izzo earthflow (southern Italy). Journal of Applied
605 Geophysics 56(1), 17-29.

606 Petiau, G., 2000. Second generation of lead-lead chloride electrodes for geophysical applications.
607 Pure and Applied Geophysics 157(3), 357-382.

608 Piegari, E., Cataudella, V., Di Maio, R., Milano, L., Nicodemi, M., Soldovieri, M.G., 2009. Electrical
609 resistivity tomography and statistical analysis in landslide modelling: a conceptual approach. Journal
610 of Applied Geophysics 68(2), 151-158.

611 Rawson, P.F., Wright, J.K., 1995. Jurassic of the Cleveland basin, North Yorkshire. In: Taylor, P.D.
612 (Ed.), Field Geology of the British Jurassic. Geological Society of London, London, UK, pp. 173-208.

613 Revil, A., Pezard, P.A., Glover, P.W.J., 1999. Streaming potential in porous media 1. Theory of the
614 zeta potential. Journal of Geophysical Research-Solid Earth 104(B9), 20021-20031.

615 Samouelian, A., Cousin, I., Tabbagh, A., Bruand, A., Richard, G., 2005. Electrical resistivity survey in
616 soil science: a review. Soil & Tillage Research 83(2), 173-193.

617 Sass, O., Bell, R., Glade, T., 2008. Comparison of GPR, 2D-resistivity and traditional techniques for the
618 subsurface exploration of the Öschingen landslide, Swabian Alb (Germany). Geomorphology 93(1-2),
619 89-103.

620 Schmutz, M., Guerin, R., Andrieux, P., Maquaire, O., 2009. Determination of the 3D structure of an
621 earthflow by geophysical methods The case of Super Sauze, in the French southern Alps. Journal of
622 Applied Geophysics 68(4), 500-507.

623 Schrott, L., Sass, O., 2008. Application of field geophysics in geomorphology: advances and
624 limitations exemplified by case studies. Geomorphology 93(1-2), 55-73.

625 Shevnin, V., Mousatov, A., Ryjov, A., Delgado-Rodriquez, O., 2007. Estimation of clay content in soil
626 based on resistivity modelling and laboratory measurements. Geophysical Prospecting 55(2), 265-
627 275.

628 Sjodahl, P., Dahlin, T., Zhou, B., 2006. 2.5D resistivity modeling of embankment dams to assess
629 influence from geometry and material properties. Geophysics 71(3), G107-G114.

630 Supper, R., Römer, A., 2003. New achievements in developing a high-speed geoelectrical system for
631 landslide monitoring. Proceedings of the 9th Meeting of Environmental and Engineering Geophysics.
632 European Association of Geoscientists and Engineers (EAGE), Prague, Czech Republic, p. O-004.

633 Telford, W.M., Geldart, L.P., Sheriff, R.E., 1990. Applied Geophysics. Cambridge University Press,
634 Cambridge, UK.

635 Van Den Eeckhaut, M., Verstraeten, G., Poesen, J., 2007. Morphology and internal structure of a
636 dormant landslide in a hilly area: the Collinabos landslide (Belgium). Geomorphology 89, 258-273.

637 Wilkinson, P., Chambers, J., Meldrum, P., Ogilvy, R., Mellor, C., 2005. A comparison of self-potential
638 tomography with electrical resistivity tomography for the detection of abandoned mineshafts.
639 Journal of Environmental and Engineering Geophysics 10, 381-389.

640 Yasukawa, K., Ishido, T., Suzuki, I., 2005. Geothermal reservoir monitoring by continuous self-
641 potential measurements, Mori geothermal field, Japan. Geothermics 34(5), 551.

642 Yilmaz, S., 2007. Investigation of Gurbulak landslide using 2D electrical resistivity image profiling
643 method (Trabzon, northeastern Turkey). Journal of Environmental and Engineering Geophysics 12(2),
644 199-205.

645

646

647

FIGURES

Fig. 1. Geological map based on the geological resurvey of the area, showing the location of the study site and the distribution of landslide deposits. Coordinate systems are given as British National Grid (bold) and latitude and longitude (normal). Inset map (top left) shows the location of the study site within the UK.

Fig. 2. (A) Geomorphological map of the study site produced from stereophotogrammetry and the interpretation of aerial LiDAR data and ground-based RTK-GPS measurements. The shaded relief base map was generated from aerial LiDAR data with vegetation included. (B) Study site plan showing geophysical survey locations, intrusive sampling points, and inferred geological boundaries derived from recent geological mapping of the area. The base map, showing topographic contours in metres above Ordnance Datum, was produced from aerial LiDAR data.

Fig. 3. Logs for selected hand auger holes (i.e. A1, A2, and A3) and boreholes (i.e. BH1, BH5, and BH7). Each log comprises a lithological (left) and stratigraphic (right) component. Lithology is given in terms of dominant material types; significant laminations (lam.) of different material types or mixed material types (e.g. sand & silt) are indicated. Sample locations are shown in Fig. 2B. Depths (z) are given in metres below ground level (bgl).

Fig. 4. 2D ERT models and associated SP profiles for lines 1, 2, 3 and 4, with key geological, geomorphological, and hydrological features marked.

Fig. 5. Apparent resistivity map (0-1 m depth profile) of study site, showing location of other geophysical surveys, intrusive sampling locations, and the toe of the landslide identified from the geomorphological map (Fig. 2A).

Fig. 6. (A) Plot of the self-potential V as a function of (x,y), including geomorphological features (black line work – see Fig. 2A for key) and arrows (white) indicating the likely direction of fluid flow; and (B) horizontal slices showing charge occurrence probability (COP) η as a function of (x,y,z) for the

672 SP mapping area. The x and y coordinates refer to a local grid with the origin located in the south-
673 western corner of the survey area.

674 Fig. 7. Vertical sections through the 3D ERT model showing the inferred thickness of slipped material
675 (dashed white lines) and geological boundaries (dotted white lines). Auger and borehole logs show
676 stratigraphic units: WMF (grey), SSF (black) and RMF (white). Detailed lithological and stratigraphic
677 logs for the labelled holes are shown in Fig. 3.

678 Fig. 8. Plan view of the 3D ERT model showing the resistivity distribution across the surface layer,
679 with intrusive sample locations (black/white circles – see Fig. 3 for detailed logs), backscarp and toe
680 locations identified from geomorphological mapping (black lines – see Fig. 2A for key), geological
681 boundary between the SSF and WMF (dotted white line), and inferred lithological boundary
682 between landslide material and bedrock (dashed white line) derived from 3D ERT model and
683 intrusive sampling. The x and y coordinates refer to a local grid with the origin located in the south-
684 western corner of the survey area.

685 Fig. 9. Integrated 3D perspective view of the study site, with a northwesterly aspect, showing the
686 resistivity models generated from lines 1 to 4 and the 3D survey area overlain by a recent aerial
687 photograph (© UK Perspectives UKP2006/01). Annotation shows interpreted solid geological
688 bedrock boundaries (dashed line), surface of separation between bedrock and slipped WMF material
689 (solid line), and the lateral extent of slipped material within the 3D ERT survey area (dotted line).

Figure 1

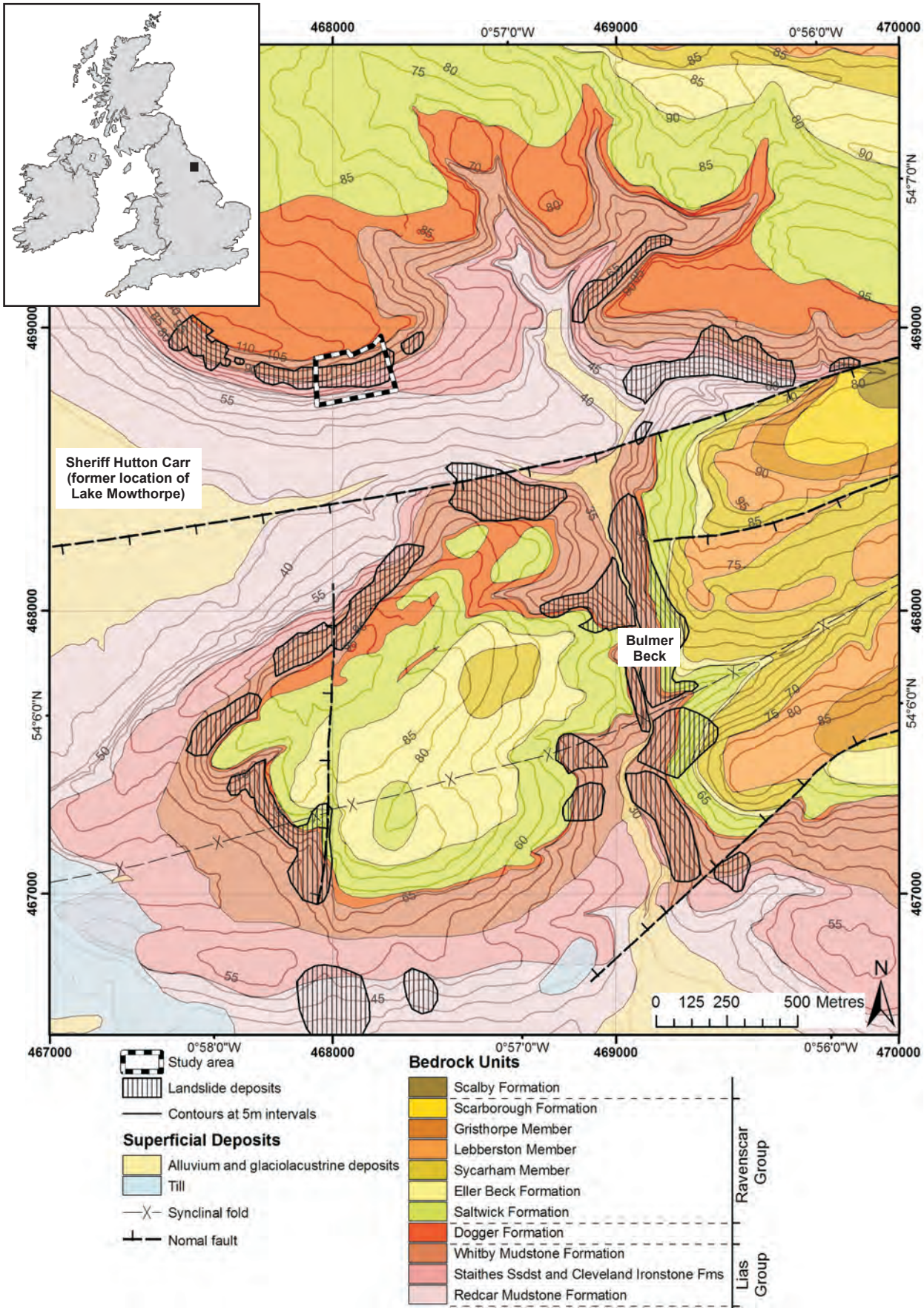
468000
0°57'0"W
469000
0°56'0"W
470000
54°7'0"N
469000
468000
54°6'0"N
467000
Sheriff Hutton Carr
(former location of
Lake Mowthorpe)
Bulmer
Beck
N
0 125 250 500 Metres
0°58'0"W
Study area
Landslide deposits
Contours at 5m intervals
Superficial Deposits
Alluvium and glaciolacustrine deposits
Till
Synclinal fold
Nomal fault
Bedrock Units
Scalby Formation
Scarborough Formation
Gristhorpe Member
Lebberston Member
Sycarham Member
Eller Beck Formation
Saltwick Formation
Dogger Formation
Whitby Mudstone Formation
Staithes Ssdst and Cleveland Ironstone Fms
Redcar Mudstone Formation
Ravenscar Group
Lias Group

Figure 2

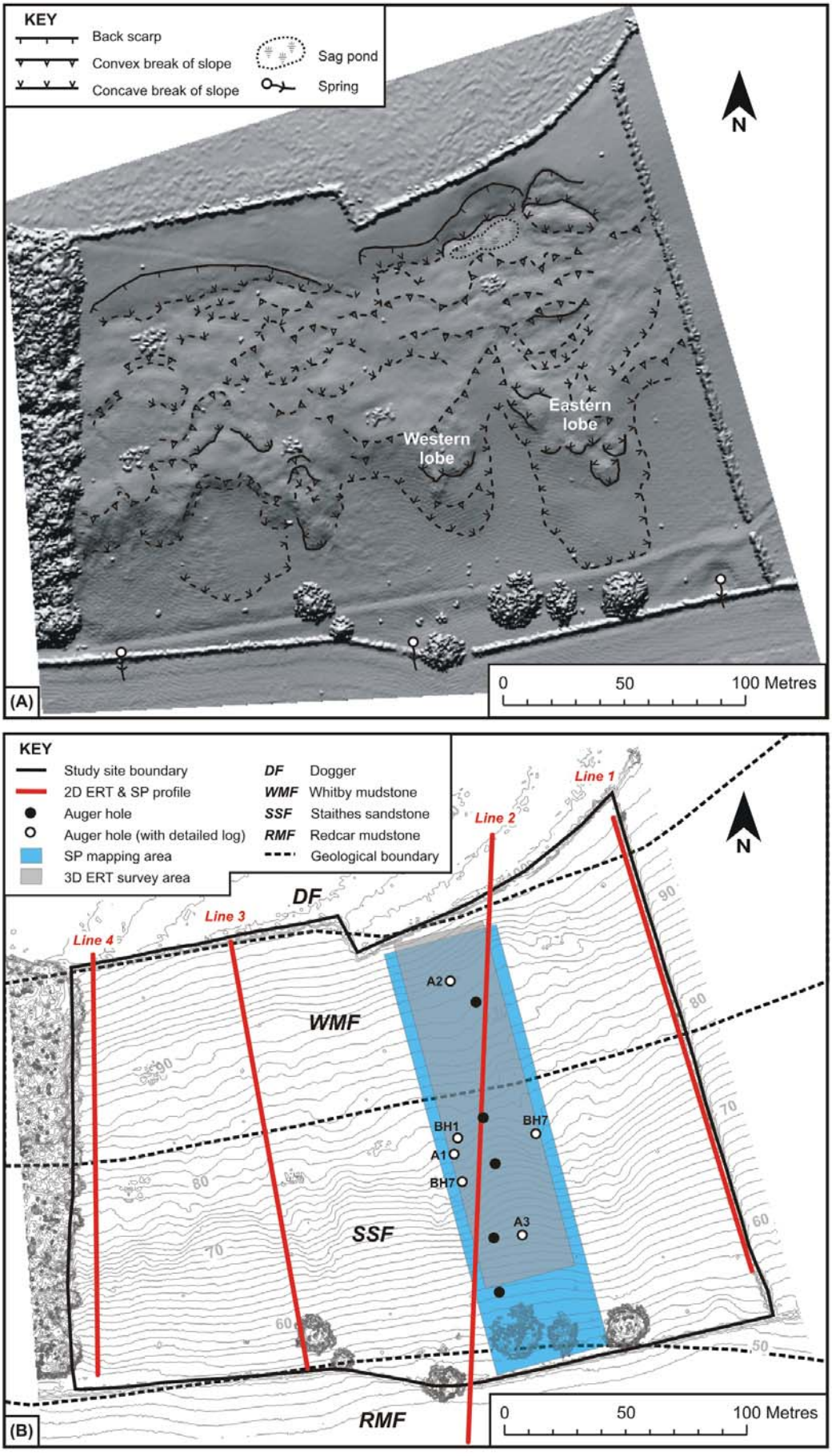
KEY
Back scarp
Convex break of slope
Concave break of slope
Sag pond
Spring
N
Western lobe
Eastern lobe
0
50
100 Metres
(A)
KEY
Study site boundary
2D ERT & SP profile
Auger hole
Auger hole (with detailed log)
SP mapping area
3D ERT survey area
DF Dogger
WMF Whitby mudstone
SSF Staithes sandstone
RMF Redcar mudstone
Geological boundary
Line 1
Line 2
Line 3
Line 4
DF
WMF
SSF
RMF
A1
A2
A3
BH1
BH7
BH7
N
90
80
70
60
50
0
50
100 Metres
(B)

Figure 3

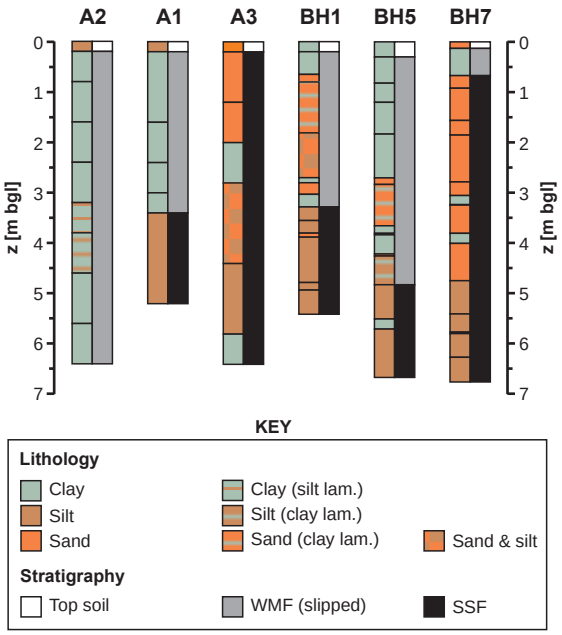
A2
A1
A3
BH1
BH5
BH7
z [m bgl]
0
1
2
3
4
5
6
7
KEY
Lithology
Clay
Silt
Sand
Clay (silt lam.)
Silt (clay lam.)
Sand (clay lam.)
Sand & silt
Stratigraphy
Top soil
WMF (slipped)
SSF

Figure 4

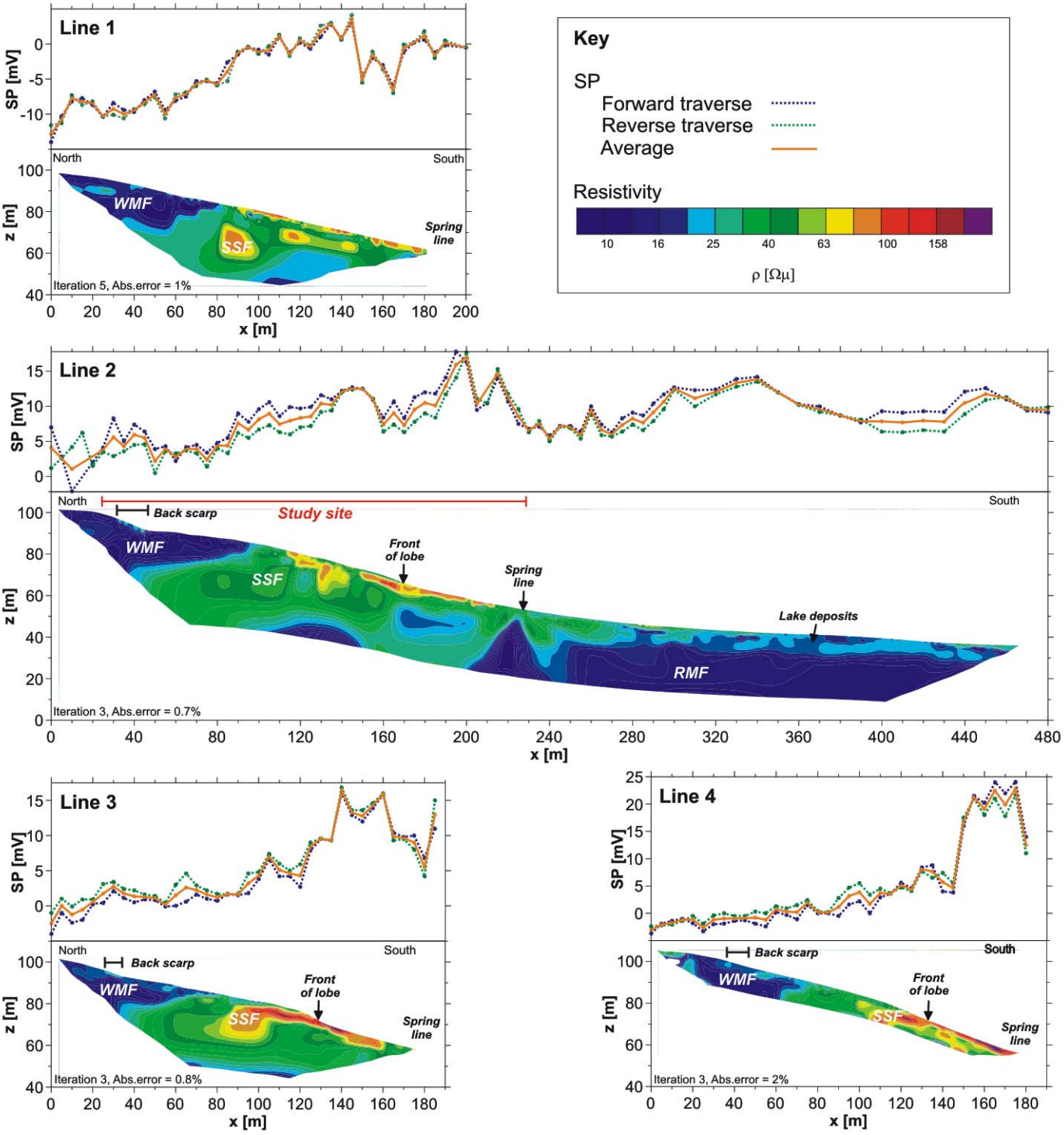
Line 1
SP [mV]
North
South
WMF
SSF
Spring line
Iteration 5, Abs.error = 1%
z [m]
x [m]
Key
SP
Forward traverse
Reverse traverse
Average
Resistivity
10 16 25 40 63 100 158
ρ [Ωμ]
Line 2
Back scarp
Study site
Front of lobe
Spring line
Lake deposits
RMF
Iteration 3, Abs.error = 0.7%
Line 3
Iteration 3, Abs.error = 0.8%
Line 4
Iteration 3, Abs.error = 2%

Figure 5

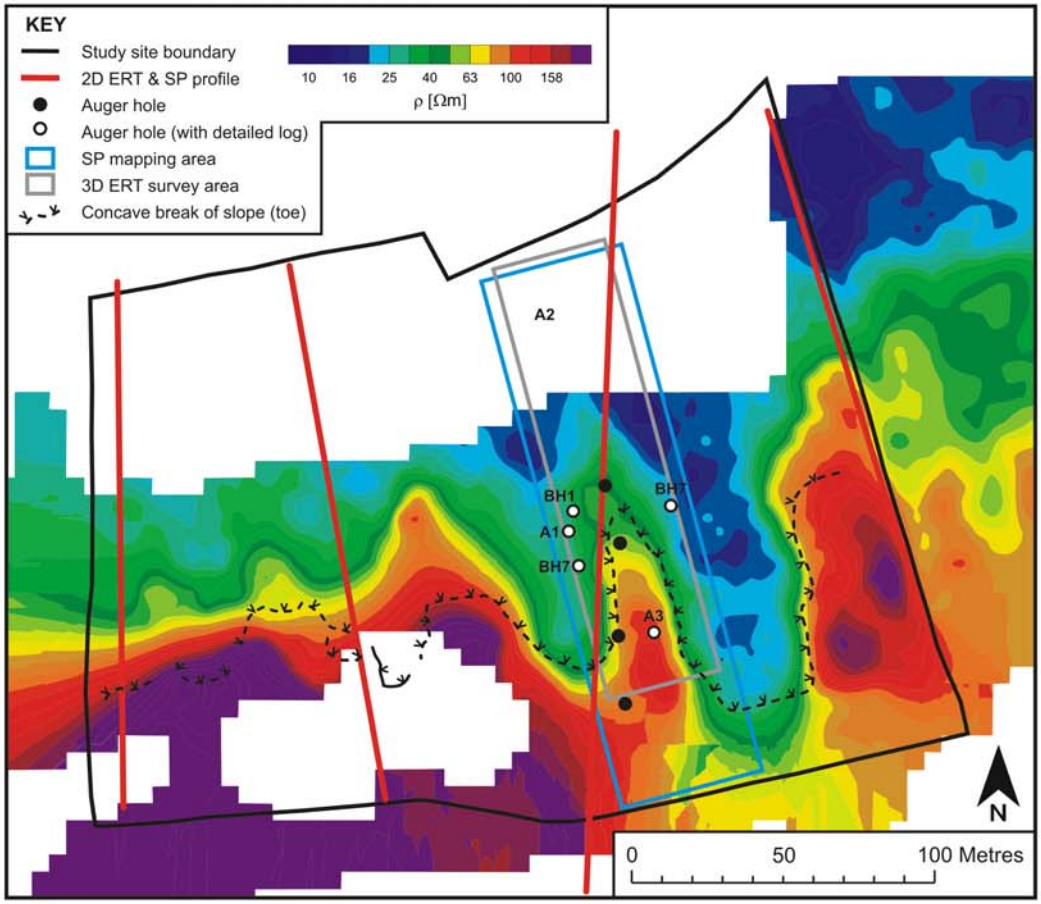
KEY
Study site boundary
2D ERT & SP profile
Auger hole
Auger hole (with detailed log)
SP mapping area
3D ERT survey area
Concave break of slope (toe)
10 16 25 40 63 100 158
ρ [Ωm]
A2
BH1
A1
BH7
BH7
A3
N
0
50
100 Metres

Figure 6

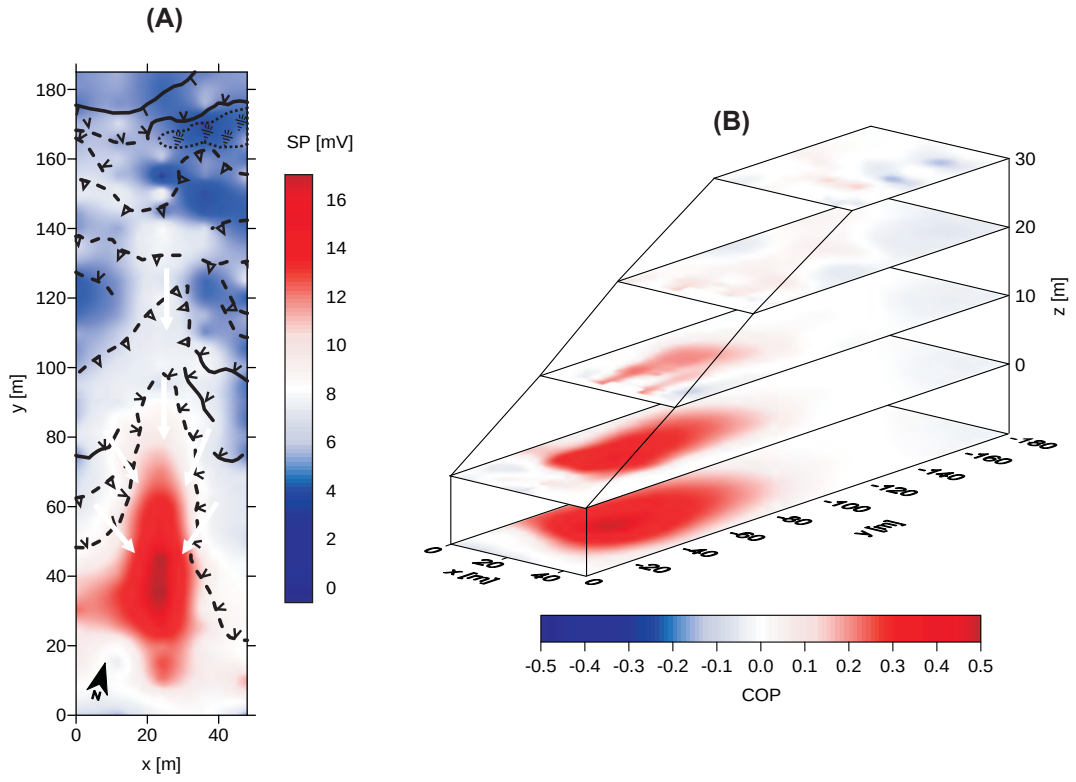
(A)
SP [mV]
16
14
12
10
8
6
4
2
0
y [m]
x [m]
0
20
40
60
80
100
120
140
160
180
N
(B)
z [m]
30
20
10
0
-160
-140
-120
-100
-80
-60
-40
-20
0
20
40
x [m]
-0.5 -0.4 -0.3 -0.2 -0.1 0.0 0.1 0.2 0.3 0.4 0.5
COP

Figure 7

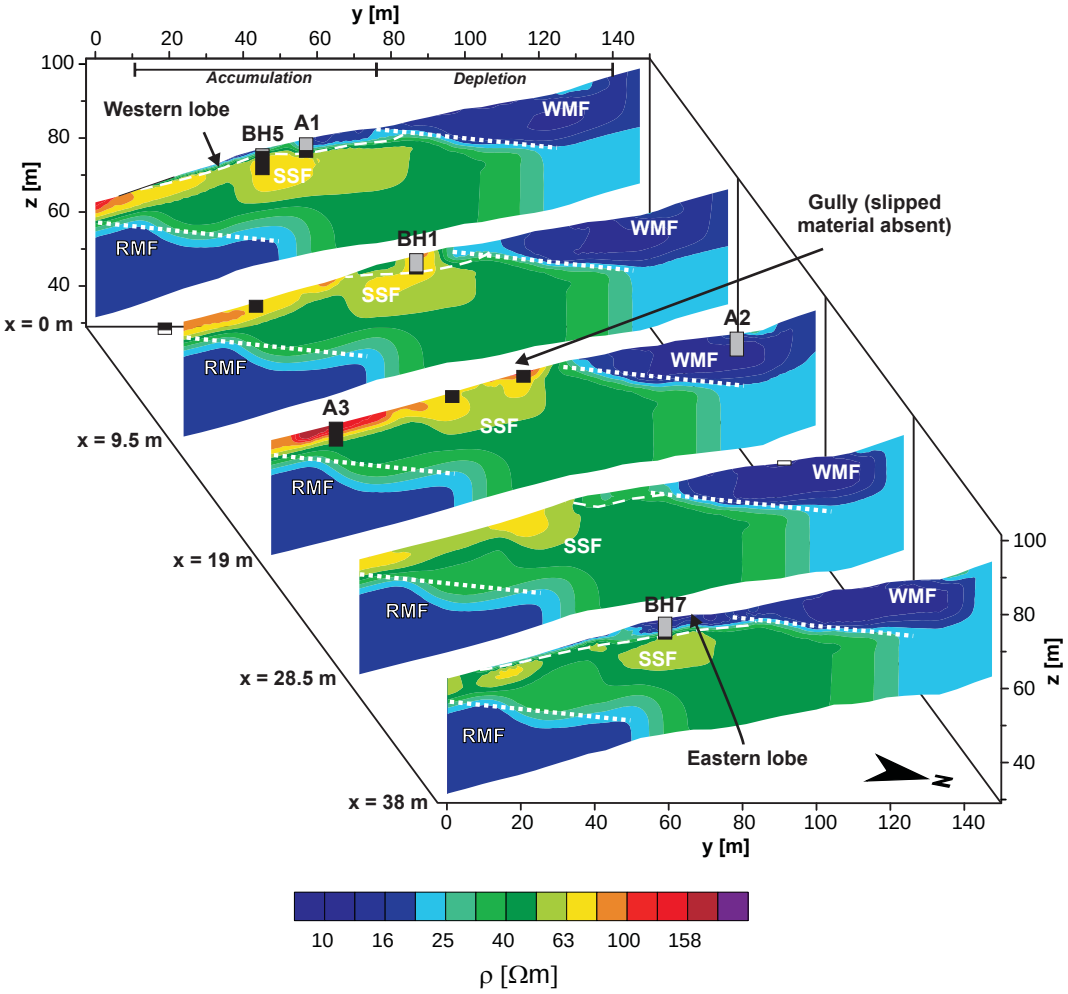
y [m]
0
20
40
60
80
100
120
140
z [m]
100
80
60
40
Accumulation
Depletion
Western lobe
BH5
A1
BH1
A2
A3
BH7
WMF
SSF
RMF
Gully (slipped material absent)
Eastern lobe
N
x = 0 m
x = 9.5 m
x = 19 m
x = 28.5 m
x = 38 m
10
16
25
40
63
100
158
ρ [Ωm]

Figure 8

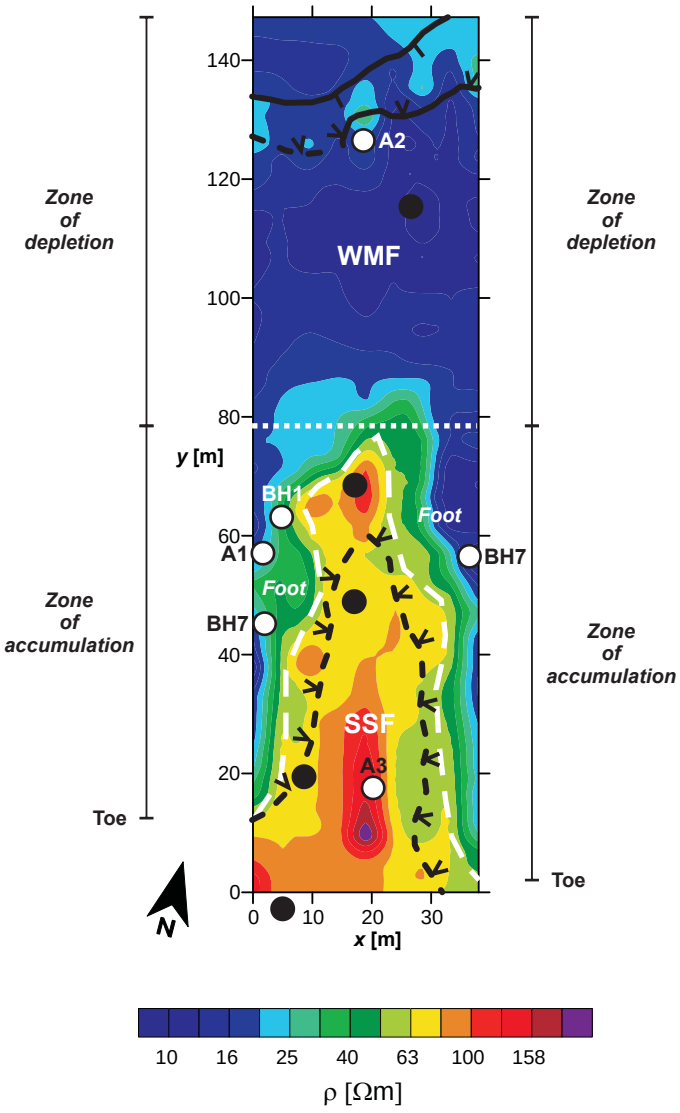
Zone of depletion
Zone of depletion
Zone of accumulation
Zone of accumulation
Toe
Toe
A2
WMF
BH1
Foot
A1
BH7
Foot
BH7
SSF
A3
y [m]
x [m]
N
0
20
40
60
80
100
120
140
0
10
20
30
10
16
25
40
63
100
158
ρ [Ωm]

Figure 9

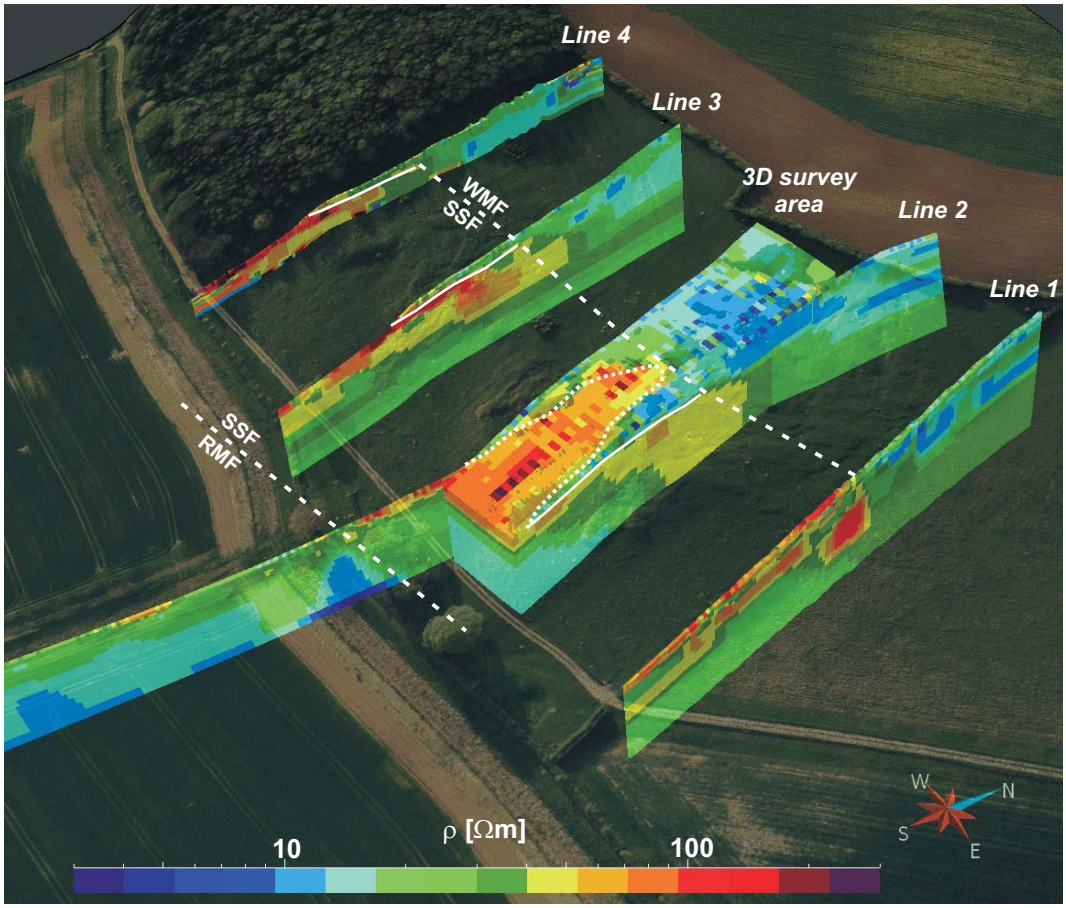
Line 4
Line 3
3D survey area
Line 2
Line 1
WMF
SSF
SSF
RMF
ρ [Ωm]
10
100
W
N
S
E